Organic chemistry influences the observed seasonal cycle of molecular oxygen on Mars

Benjamin Taysum[1,1,1,1], Paul Palmer[1,1,1], and Paul Palmer[1]

[1]University of Edinburgh

November 30, 2022

Abstract

Recent measurements collected by the Mars Curiosity Rover at the Gale Crater revealed an unexpectedly large seasonal cycle of molecular oxygen (O2). We use a 1-D photochemical model, including inorganic and organic chemistry, and its adjoint model to quantify the sensitivity of changes in O2 to changes in inorganic and organic compounds. We show that O2 changes are most sensitive to changes in organic compounds from the oxidation of methane. We find that an accelerated loss of atmospheric methane, achieved either by increasing the atmospheric loss or by imposing an additional surface loss, does not reconcile model and observed values of O2 but it helps to explain the O2 seasonal variation. The resulting changes in atmospheric composition are below the detection limits of orbiting instruments.

Organic chemistry influences the observed seasonal cycle of molecular oxygen on Mars

Benjamin M. Taysum,[1,2*] Paul I. Palmer,[1,2]

[1]School of GeoSciences, University of Edinburgh, Edinburgh, UK
[2]Centre for Exoplanet Science, University of Edinburgh, Edinburgh, UK

[*]To whom correspondence should be addressed; E-mail:Ben.Taysum@ed.ac.uk.

Recent measurements collected by the Mars Curiosity Rover at the Gale Crater revealed an unexpectedly large seasonal cycle of molecular oxygen (O_2). We use a 1-D photochemical model, including inorganic and organic chemistry, and its adjoint model to quantify the sensitivity of changes in O_2 to changes in inorganic and organic compounds. We show that O_2 changes are most sensitive to changes in organic compounds from the oxidation of methane. We find that an accelerated loss of atmospheric methane, achieved either by increasing the atmospheric loss or by imposing an additional surface loss, does not reconcile model and observed values of O_2 but it helps to explain the O_2 seasonal variation. The resulting changes in atmospheric composition are below the detection limits of orbiting instruments.

Atmospheric observations of methane (CH_4) on Mars, often considered an indicator of microbial life, have long since been a source of curiosity and controversy. Over the past two decades, CH_4 observations have been reported by orbiting satellites (*1–3*), ground-based telescopes (*4–6*), and by *in situ* measurements at Gale Crater by the Curiosity Rover (*7*). A five-

year analysis of Curiosity CH_4 measurements from the Sample Analysis at Mars (SAM) suite revealed variations indicative of a seasonal cycle (*8*), but more data are needed to confirm this cycle (*9*). However, other data, including recent orbiting instruments, have failed to detect atmospheric CH_4 (*10,11*). Observed variations of CH_4, from the Curiosity Rover team or collectively via the range of measurements, are arguably more unexpected than the presence of CH_4. They would suggest, for example, an atmospheric loss process that is faster than known atmospheric chemistry or an unrealistic population of surface methanotrophic organisms. Either scenario potentially overwhelms the atmospheric redox budget (*12*).

Atmospheric photochemical models of Mars estimate the photochemical lifetime of CH_4 to be $>$250 years below altitudes 70 km (*13–16*). Given characteristic atmospheric transport timescales, this photochemical lifetime suggests that Martian CH_4 should be well-mixed throughout the atmosphere. Reconciling models and data either requires an atmospheric loss process that corresponds to a lifetime shorter than 200 days (*13, 16*) or a lifetime of the order of one hour against a surface loss process. The known atmospheric losses below 70 km for CH_4 are oxidation by atomic oxygen ($O(^3P)$, $O(^1D)$) and the hydroxyl radical (OH), resulting in the production of methyl and methoxy radicals (CH_3, CH_3O). Recent analysis of molecular oxygen (O_2) measurements from the tunable diode laser aboard the SAM at Gale Crater revealed an unexpectedly large seasonal variation of O_2 (*17*) that cannot be reproduced by current photochemical models. During the Northern hemisphere's Autumn and Winter periods, observed values of O_2 decreased by 23% over a 38-sol period, consistent with a lifetime of approximately 150 days which is much shorter its expected photochemical lifetime of 10 years (*18*). Knowledge of O_2 photochemistry can not currently be reconciled with observed variations in O_2. Limitations to current knowledge of the chemical and physical properties of Martian soil precludes any definite explanation for observed variations of O_2. Consequently, the current suite of Martian CH_4 and O_2 measurements present a conundrum: can we reconcile observed

variations of CH_4 and O_2, related by photochemistry, without overwhelming the atmospheric redox chain?

Here, we use a 1-D atmospheric photochemistry model of Mars (*16*) to study the influence of reactive inorganic and organic gas-phase chemistry on CH_4 and O_2 and to interpret observed SAM measurements of O_2. To achieve this, we calculate the tangent linear model (TLM) and its adjoint of the 1-D model, both common approaches to study the physics and chemistry of Earth's atmosphere (*19, 20*). The TLM describes the first derivative of the time-dependent photochemical model, e.g. what is the sensitivity of O_2 to a change in trace gas A? A more elegant approach is to use the adjoint of the TLM that allows us to ask the question: which inorganic and organic trace gases are responsible for an observed change in O_2? The 1-D photochemical model, with vertical resolutions ranging from 10–100 m below 1 km and 1–10 km up to an altitude of approximately 70 km, uses pre-calculated half-hourly values for physical atmospheric parameters such as surface pressure, temperature, wind, and turbulent kinetic energy profiles from the Mars Climate Database v5.3 (MCDv5.3) (*21*), interpolated to the location of Gale Crater (4.5° S, 137.4° E). We also initialise the model with mixing ratio profiles of CO_2, CO, O_2, H_2O vapour, and H_2 from the MCDv5.3 dataset, and with a uniform profile of 50 ppt of CH_4 which is consistent with current observations (*11*). For each solar longitude (L_s) we report, we spin-up the model over 110 sols to generate steady-state values for longer-lived chemical species, e.g. H_2O_2, formaldehyde (HCHO), and methy hydroperoxide (CH_3OOH). We then run the TLM and its adjoint model over three successive sols and report those results.

Figure 1a,b shows the sensitivity of surface O_2 VMR at Gale Crater to changes in O_3, H_2O vapour, H_2O_2 and H_2, and to changes in CH_4 and a subset of its oxidation products (HCHO, CH_3OOH, and CH_3OH). With the exception of O_3, we find that O_2 is negatively sensitive to changes in inorganic and organic precursors, with peak values at or below 1 km as expected

given the two-sol time period. Sensitivities are generally largest at L_S=133° when the water vapour content in the column above Gale Crate (4.5° South, 137.4° East) reaches its seasonal maximum. This also coincides with the time at which the optical opacity of the Martian atmosphere (determined primarily by dust) is at its lowest, prior to the seasonal rise occurring at a solar longitude of approximately 145° (*22*).

Generally, we find that surface O_2 at Gale Crater is more sensitive to changes in HCHO and CH_3OOH, two key oxidation products of CH_4, than either H_2O_2 and water vapour. This sensitivity corresponds to an initial state with 50 ppt CH_4 (*11*). In comparison, the sensitivity of O_2 to changes in CH_4 using our control chemical network (*16*) is much smaller due to its longer chemical lifetime that exceeds 200 years (*16*). The large sensitivity of O_2 to changes in CH_4 oxidation products, coupled with the need for a faster CH_4 (physical, chemical, or biological) loss process to reconcile with Rover CH_4 measurements (*13*), leads us to examine how O_2 would respond to an accelerated loss process close to the Martian surface. To investigate this we force atmospheric CH_4 to have a lifetime of one hour below 400 m. We accomplish this by including a reaction that splits CH_4 into atomic hydrogen and the CH_3 radical, mimicking the photolysis of CH_4 that is only efficient above 60 km and electrochemical reactions that could results from dust charging due to wind saltation, dust devils and dust storms (*23, 24*). We find that this accelerated (seasonally invariant) loss of CH_4 only affects the sensitivity of O_2 to changes in CH_4, as expected, which increases by four orders of magnitude ($O(10^{-1})$) at all solar longitudes. There is no route in the chemical network to recover CH_4 from its oxidation products so their relationship to O_2 remains the same. SAM has previously measured variations in CH_4 at Gale Crater of the magnitude 10^{-10}–10^{-9} mol/mol (*17*). Based on our sensitivity calculation, an increase of 10% in CH_4 would result in a decrease in O_2 of 10^{-11}–10^{-10} mol/mol. Our calculations suggest that surface O_2 is as sensitive to CH_4 released two sols prior as its inorganic precursors (Fig. 1a). Our results also suggest that a large surface loss for

CH_4, which would reconcile photochemical models with measurements, would have significant implications for the seasonal cycle of O_2.

Figure 2 shows the relationship between the lifetime of atmospheric CH_4 and O_2 at Gale Crater. We initialise CH_4 in the first model layer in our calculations using measured season-specific values (*8*) (Fig. 2a). Using our approach to describe the accelerated CH_4 loss, we define the lifetime of CH_4 below 400 m from 15 mins to one week during daylight (solar zenith angle $>95^\circ$) that reverts back to the standard chemical network in the absence of sunlight. Our spin-up period from these conditions is 110 sols, which is much longer than the vertical mixing timescale ($\simeq$ 2 sols). Fig. 2a shows the change in the CH_4 column loss below 400 m, which increases by several orders of magnitude from the control value of 10^3 molec cm^{-2} s^{-1} as the lifetime decreases. Fig. 2b shows that the corresponding column lifetime of O_2 in lowest 10 km is significantly decreased ($>$ factor of three) by small (ppb) increases in CH_4 in the surface layer due to an accelerated surface loss process. The largest absolute change in O_2 lifetime is during northern spring (L_S = 0–90°) when the SAM CH_4 values are highest (Fig. 2a) and the O_2 loss is largest (Fig. 2c), and the small absolute change is during northern summer (L_S = 90–180°) when the O_2 loss is smallest (Fig. 2c). Fig. 2d shows observed surface O_2 values at Gale Crater measured by SAM (*17*), and the steady-state O_2 values at noon (local time of 12:00) at the surface as calculated by the 1-D chemistry model, defined as the ratio of the photochemical production of O_2 (molec cm^{-3} s^{-1}) and the photochemical loss of O_2 (s^{-1}), normalised by atmospheric number density to convert to VMR units. We acknowledge this approach is an approximation because of the long lifetime of O_2 and our inability using our 1-D model to properly describe deviations from zonal mean transport, but our method does provide some indication of how changes in CH_4 chemistry will impact O_2. We find that an accelerated organic chemistry network cannot explain the additional O_2 needed to reconcile with the SAM observations. We find that an O_2 lifetime of $\simeq$1000 sols is required to reconcile our photochemical

model with SAM O_2 observations at L_S=140° in Mars Year 33 (*17*), corresponding to a CH_4 loss of $>10^{10}$ molecules cm^{-2} s^{-1}. This CH_4 loss rate is unachievable with the SAM CH_4 observations, irrespective of the CH_4 lifetime we prescribe. Achieving this loss flux of CH_4 would require a larger ppb-level abundance of CH_4.

Figure 3 compares the SAM and photochemical model O_2 values at Gale Crater, corresponding to Fig. 2d, but with values normalized by the corresponding observed or model value at L_S = 345° We find that the best agreement between seasonal model and measured O_2 values, using SAM measured CH_4 VMRs at the surface (*7*), corresponds to a CH_4 lifetime shorter than two hours during L_S = 0–75°, increasing to 2–12 hours during L_S = 75–135°, before decreasing to less than two hours during L_S = 135–360°. These changes to the chemical network result in better agreement with the observed O_2 seasonal cycle, relative to our control run, during solar longitudes 90° – 180°. An additional requirement to reconcile SAM measurements with photochemistry models is the addition of 10^{20} O_2 molecules cm^{-2} to the column between L_S 60–140° (*17*). We find that the accelerated organic chemistry network cannot increase the rate at which O_2 is produced and therefore cannot be responsible for this additional O_2 that is missing from current photochemical models (Fig. 2d). A speculative scenario that would help reconcile the magnitude and seasonal variation of photochemical model and the SAM O_2 observations is a seasonally-varying CH_4 loss process that peaks during the dusty season when optical opacity is highest (L_S = 150–10°, Fig. 3b) that would suppress the net production of O_2 from additional seasonally-invariant near-surface source. During periods when the optical opacity is at a minimum, i.e. outside the dust season, the combination of an active O_2 source and a lower rate of destruction for CH_4 could result in an additional 10^{17}–10^{18} molecules cm^{-2} sol^{-1} that would accumulate to 10^{20} O_2 molecules cm^{-2} within 100 sols. Previous laboratory studies have proposed mechanisms that would allow dust to remove CH_4 from the atmosphere (*25–27*), but there is still a great deal that we do not understand about airborne dust on Mars.

An accelerated organic chemistry network would also increase the production of trace gases that are observable from the Trace Gas Orbiter. Formaldehyde, for example, would be present at 0.1–1 ppb levels below 2 km, exceeding the instrument detection limits for the Atmospheric Chemistry Suite during low dust periods (0.17 ppb) but not during high dust periods (1.7 ppb) (*28*). The Nadir and Occultation for MArs Discovery instrument is capable of detecting 0.03 ppb of HCHO during solar occultations with a signal-to-noise ratio of 3000 (*29*), which the model predicts at altitudes of 2.5–4 km, a region that is difficult to observe using solar occultation because of dust along the observed limb. If the accelerated network was driven exclusively by a surface loss process, the resulting CH_4 and O_2 perturbations would be mainly limited to the lowest 5 kms and would likely evade detection by satellite observations thereby reconciling results from recent satellite and *in situ* measurements.

Altering the speed at which photochemistry takes place on Mars will have implications of the redox budget (*12*), which demands a balance with our new source of oxidising power that is ten times stronger than is available with current knowledge. We also have to consider that the discrepancy between SAM O_2 observations and our standard photochemical model reflects an unknown physical or chemical process that is unrelated to CH_4 (*17*), and that the similar seasonal cycles are a coincidence. If this uncharacterized physical or chemical process acts as a source of O_2 then the accelerated CH_4 chemical network close to the Martian surface coupled with said process could help in coinciding the true O_2 VMRs measured by SAM and the strength of the O_2 cycle at Gale Crater, and these missing sources may act as a source for the redox budget balancing required for the chemical loss of CH_4. Although several Martian surface loss processes for CH_4 have been proposed (*26, 27, 30*), we have taken a process-agnostic approach by prescribing the resulting change in CH_4 lifetime. The presence of perchlorates (ClO_4^-) within the Martian soil (*31*) is a possible surface source for O_2 at Gale Crater via radiolysis (*32*). However, radiation levels at the Martian surface are insufficient to reproduce observed O_2 values

and this proposed O_2 source would need to be accompanied by fluxes of hydrogen and chlorine which have not been observed on Mars to date. Regolith diffusion of atmospheric H_2O_2 has also been proposed to emit surface O_2 (*33*). Atmospheric H_2O_2 is present in the Martian atmosphere at ppb levels (*34*) so the production rate of O_2 would have to be exceptionally fast.

Our calculations not only show that organic chemistry has a role to play in understanding changes in O_2 but also a better understanding of Martian soil and dust could potentially play a key role in helping to reconcile observed changes in CH_4 and O_2. Data from instruments aboard the recently landed NASA Perseverance Rover will provide valuable data regarding the geology and surface at Jezero Crater (*35*). The Mars Environmental Dynamics Analyzer (*36*) aboard Persevereance aims to further study and parameterize Martian dust size and shapes, vital for the modelling of gas-particle heterogeneous chemistry, and numerous instruments aboard aim to study the mineralogy of the surface which will provide greater understandings of possible atmosphere-surface interactions.

References

1. V. Formisano, S. Atreya, T. Encrenaz, N. Ignatiev, M. Giuranna, *Science* **306**, 1758 (2004).

2. A. Geminale, V. Formisano, M. Giuranna, *Planetary and Space Science* **56**, 1194 (2008).

3. M. Giuranna, *et al.*, *Nature Geoscience* (2019).

4. V. A. Krasnopolsky, J. P. Maillard, T. C. Owen, *Icarus* **172**, 537 (2004).

5. M. J. Mumma, *et al.*, *Science* **323**, 1041 (2009).

6. G. Villanueva, *et al.*, *Icarus* **223**, 11 (2013).

7. C. R. Webster, *et al.*, *Science* **347**, 415 (2015).

8. C. R. Webster, *et al.*, *Science* **360**, 1093 (2018).

9. E. Gillen, P. B. Rimmer, D. C. Catling, *Icarus* **336**, 113407 (2020).

10. V. A. Krasnopolsky, *Icarus* **217**, 144 (2012).

11. O. Korablev, *et al.*, *Nature* **568**, 517 (2019).

12. K. Zahnle, R. S. Freedman, D. C. Catling, *Icarus* **212**, 493 (2011).

13. F. Lefèvre, F. Forget, *Nature* **460**, 720 (2009).

14. A. S. Wong, S. K. Atreya, *Advances in Space Research* **33**, 2236 (2004). Mercury, Mars and Saturn.

15. A.-S. Wong, S. K. Atreya, T. Encrenaz, *Journal of Geophysical Research: Planets* **108** (2003).

16. B. M. Taysum, P. I. Palmer, *Journal of Geophysical Research: Planets* **125**, e2020JE006491 (2020).

17. M. G. Trainer, *et al.*, *Journal of Geophysical Research: Planets* **124**, 3000 (2019).

18. S. Atreya, Z. Gu, *Advances in Space Research* **16**, 57 (1995). The Atmospheres of Venus and Mars.

19. R. M. Errico, T. VukiEvi, K. Raeder, *Tellus A: Dynamic Meteorology and Oceanography* **45**, 462 (1993).

20. S. Frolov, *et al.*, *Monthly Weather Review* **146**, 2247 (2018).

21. E. Millour, *et al.*, *EGU General Assembly Conference Abstracts* (2017), vol. 19 of *EGU General Assembly Conference Abstracts*, p. 12247.

22. M. T. Lemmon, *et al.*, *Icarus* **251**, 96 (2015). Dynamic Mars.

23. T. L. Jackson, W. M. Farrell, G. T. Delory, J. Nithianandam, *Journal of Geophysical Research: Planets* **115** (2010).

24. J. F. Kok, N. O. Renno, *Geophysical Research Letters* **36** (2009).

25. S. J. Knak Jensen, *et al.*, *Icarus* **236**, 24 (2014).

26. R. Gough, *et al.*, *Planetary and Space Science* **59**, 238 (2011). Methane on Mars: Current Observations, Interpretation and Future Plans.

27. H. J. Jakobsen, *et al.*, *The Journal of Physical Chemistry C* **120**, 26138 (2016).

28. O. Korablev, *et al.*, *Space Sci. Rev.* **214**, 7 (2018).

29. A. C. Vandaele, *et al.*, *Space Sci. Rev.* **214**, 80 (2018).

30. S. K. Atreya, P. R. Mahaffy, A.-S. Wong, *Planetary and Space Science* **55**, 358 (2007). Planet Mars II.

31. B. Sutter, *et al.*, *Journal of Geophysical Research: Planets* **122**, 2574 (2017).

32. R. C. Quinn, *et al.*, *Astrobiology* **13**, 515 (2013). PMID: 23746165.

33. J. Lasne, *et al.*, *Astrobiology* **16**, 977 (2016). PMID: 27925795.

34. Encrenaz, T., *et al.*, *A&A* **578**, A127 (2015).

35. K. A. Farley, *et al.*, *Space Sci. Rev.* **216**, 142 (2020).

36. J. A. Rodriguez-Manfredi, *et al.*, *3rd International Workshop on Instrumentation for Planetary Mission* (2016), vol. 1980, p. 4114.

37. M. D. Smith, M.-P. Zorzano, M. Lemmon, J. Martn-Torres, T. Mendaza de Cal, *Icarus* **280**, 234 (2016). MicroMars to MegaMars.

Acknowledgments

Include acknowledgments of funding, any patents pending, where raw data for the paper are deposited, etc.

Supplementary materials

Materials and Methods

Supplementary Text

Figs. S1 to S4

References

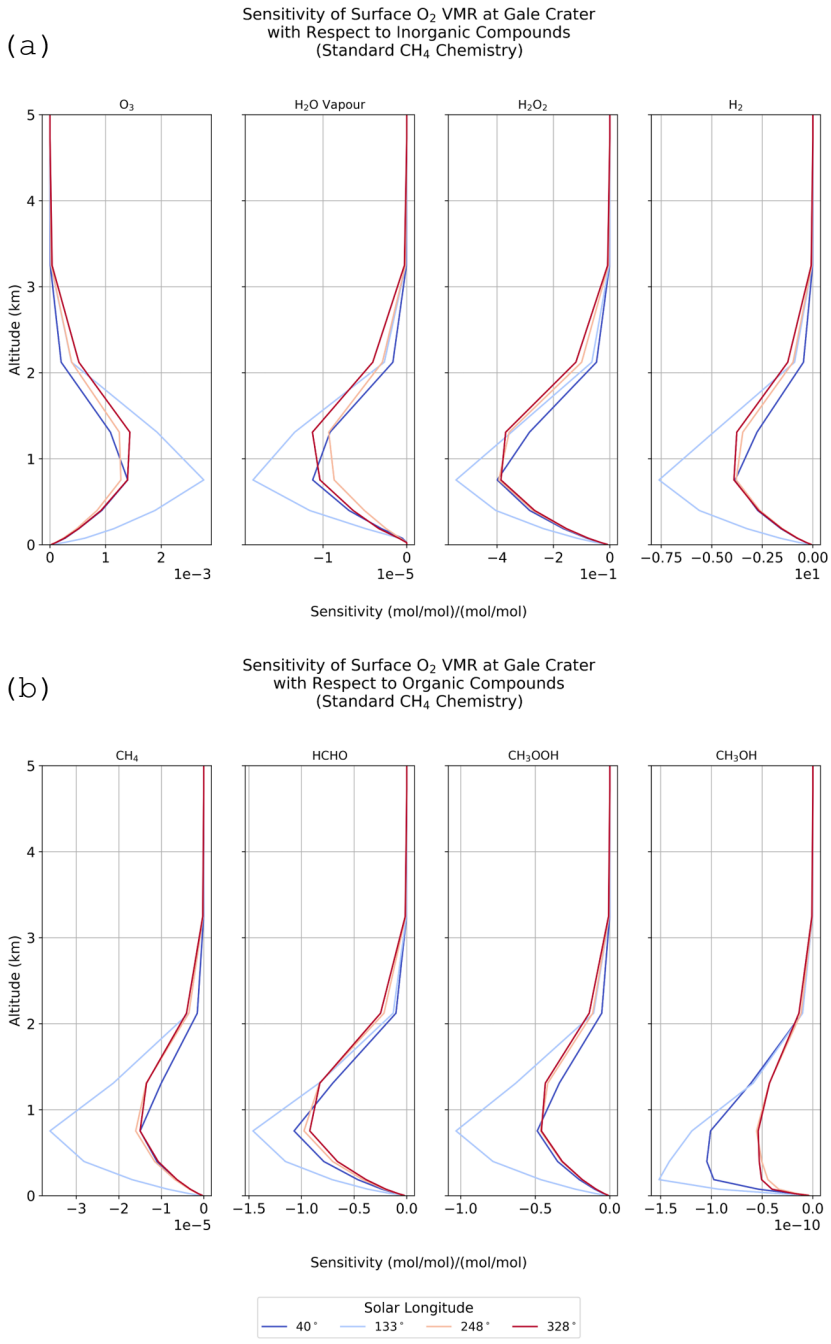

Figure 1: Sensitivity ((mol/mol)/(mol/mol)) of surface O_2 volume mixing ratios at Gale Crater to changes in a) inorganic (O_3, H_2O vapour, H_2O_2 and H_2) and b) organic (CH_4, HCHO, CH_3OOH, and CH_3OH) compounds within our control photochemical model. All calculations are reported at a local time of 00:00, and initialised uniformly with 50 ppt of CH_4 two sols prior at local noon. Different lines denote calculations evaluated at various solar longitudes along the seasonal cycle: 40°, 122°, 248°, and 328°.

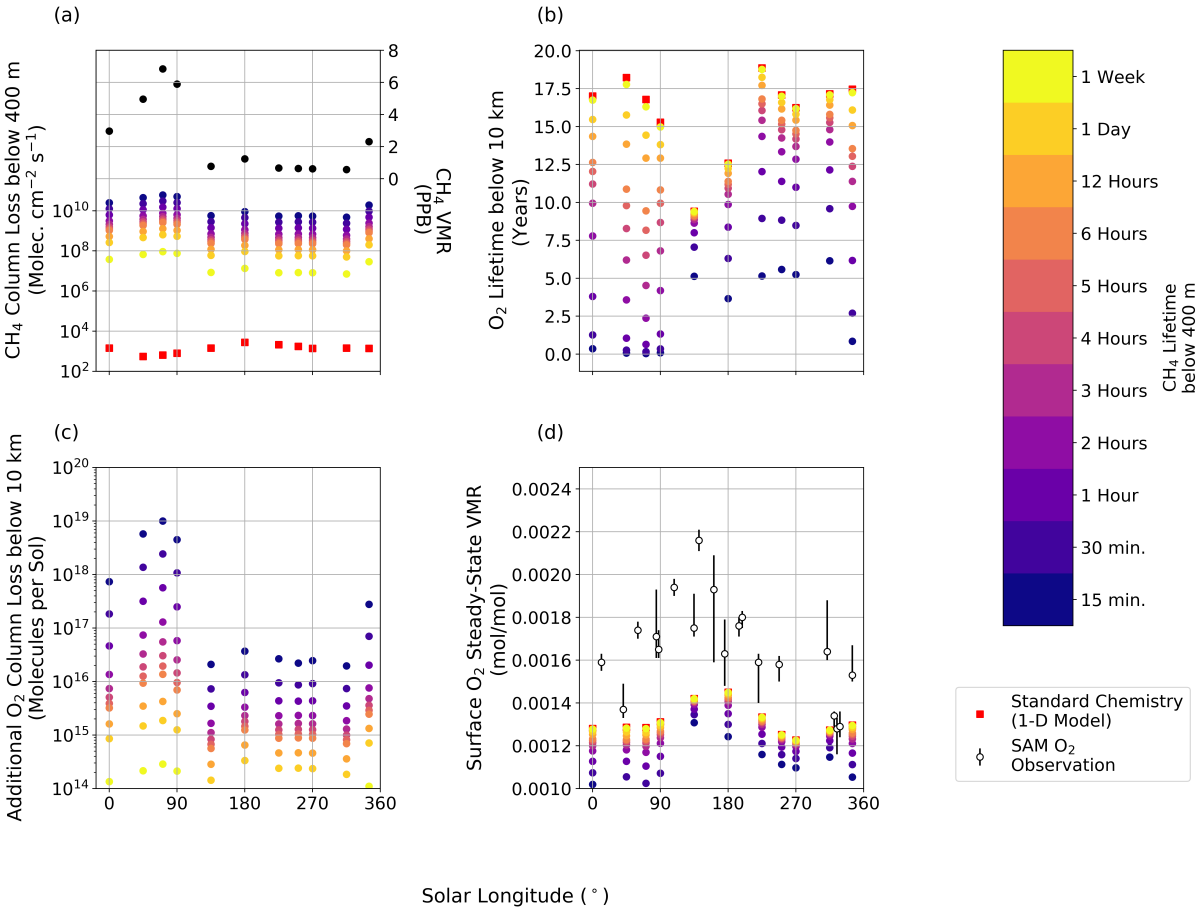

Figure 2: The impacts of including an accelerated photochemical surface sink for CH_4 on O_2 at Gale Crater on the a) O_2 chemical lifetime (years) below 10 km; (b) loss flux of CH_4 below 400 m (molecules cm^{-2} s^{-1}) that is influenced by prescribing the observed seasonal cycle of CH_4 VMR during MY 32–33 (*8*); (c) additional O_2 loss below 10 km per sol (molecules sol^{-1}); and (d) observed and model steady-state O_2 VMRs at the surface of Gale Crater.

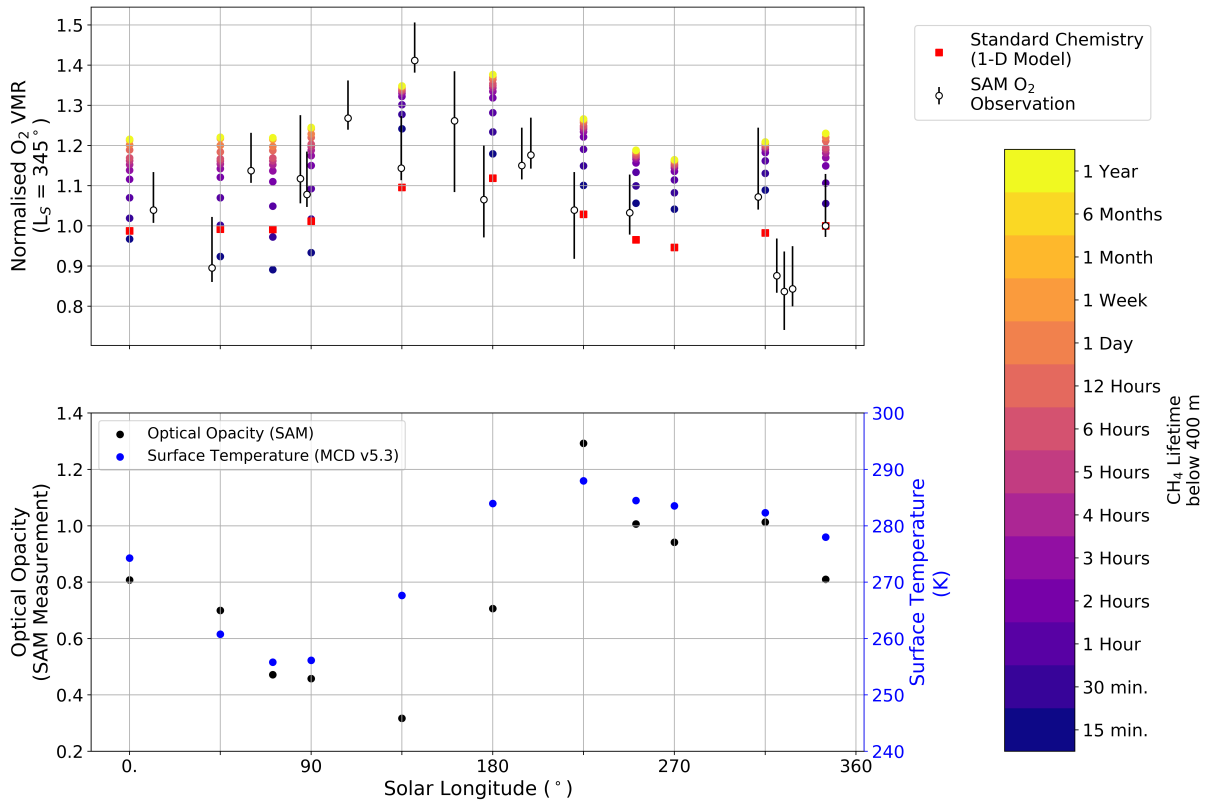

Figure 3: (a) Observed and model seasonal cycle of O_2 at the surface of Gale Crater, normalized by observed and model values at L_S = 345°. Model values correspond to the standard photochemical network and to the network that corresponds to a prescribed CH_4 lifetime below 400 m. (b) Observed optical opacity from MY 32–33 (*37*) and model surface temperature (K) (*21*).

Organic chemistry influences the observed seasonal cycle of molecular oxygen on Mars

Benjamin M. Taysum,[1,2*] Paul I. Palmer,[1,2]

[1]School of GeoSciences, University of Edinburgh, Edinburgh, UK
[2]Centre for Exoplanet Science, University of Edinburgh, Edinburgh, UK

[*]To whom correspondence should be addressed; E-mail:Ben.Taysum@ed.ac.uk.

This PDF file includes:

1 Materials and Methods

1.1 Tangent Linear Model and Adjoint Proofs

We use the adjoint of the tangent linear model (TLM) to determine the sensitivity of trace gas A at time t to changes in photochemically-related gases at prior times. Here, we document the TLM and its adjoint and provide an assessment of its accuracy.

Fully Integrated Model Equations

The 1-D model performs time-dependent calculations of tracer mass mixing ratios (MMRs) across discrete altitude steps, denoted by $\vec{PQ}$, using Equation 1.

$$\frac{\partial PQ_{i,l}}{\partial t} = P_{i,l} - L_{i,l} - \frac{\partial \phi_{i,l}}{\partial z} \tag{1}$$

Vertical diffusion, determined by vertical diffusive fluxes $\phi_{i,l}$ of species i at model layer l within the 1-D photochemistry model, is governed by the classical diffusion equation (*1*); we refer the reader to (*2*) for further details about the turbulent mixing routines. Photochemistry routines calculate the production and loss terms, $\mathrm{P}_{i,l}$ and $\mathrm{L}_{i,l}$ respectively, of each chemistry species.

Model calculations are discretised across space and time in altitude and physical timesteps denoted by Δz and Δt_p, respectively. We use 48 physical time steps (1800 s) per Martian sol, and altitude steps of less than 0.5 km below an altitude of 2 km that progressively increase to 10 km above an altitude of 20 km, following our previous work (*3*)

The stiffness of the discretised photochemistry equations is decreased by using a chemistry sub-timestep Δt_c of 600 s, corresponding to three sub-timesteps per physical timestep (*3*). The discretised form of Equation 1 is denoted by the 1-D model function F_{1D}:

$$\frac{\Delta PQ_{i,l}}{\Delta t_p} = F_{1D}(\vec{PQ}) = \Delta t_p^{-1}\Big(\Delta PQ_{i,l}^{Chem}(\vec{PQ}) - \Delta PQ_{i,l}^{Diff}(\vec{PQ})\Big), \tag{2}$$

where Δt_p denotes the timestep of the perturbation. Below we devote individual sections to the details of the diffusion (*Diff*) and chemistry (*Chem*) components.

Tangent Linear Model

The TLM of a mathematical function, such as $\mathrm{F}_{1D}(\vec{PQ})$ (Equation 2), is a linearized version of the perturbation $\Delta\vec{PQ}^{t}$ around the control state $\vec{PQ}_{C}^{t}$. The TLM is calculated using the Gateaux differentiation of Equation 2, which is first rearranged to form Equation 3:

$$G(\vec{PQ}) = \frac{\Delta\vec{PQ}}{\Delta t_p} - F_{1D}(\vec{PQ}) = 0 \quad , \tag{3}$$

First, we define a control model run, initialised with a tracer MMR vector $\vec{PQ}^{t=0} = \vec{PQ}_{C}^{t=0}$, and a model run with an initial MMR vector $\vec{PQ}^{t=0} = \vec{PQ}_{P}^{t=0}$ which is a perturbation of the control state such that $\vec{PQ}_{P}^{t} = \vec{PQ}_{C}^{t} + \vec{PQ}^{t}$". These two model runs allows us to use the Gateaux expansion (Eq. 3) for the perturbed state around the control state, defined by Equation 4 and 5, for a vector of scalars $\vec{\lambda}$:

$$G(\vec{PQ}_{C} + \vec{PQ}") - G(\vec{PQ}_{C}) = \Delta G \tag{4}$$

$$\Delta G = \frac{d}{d\vec{\lambda}} G(\vec{PQ}_{C} + \vec{\lambda}\vec{PQ}") \mid_{\lambda_\forall = 0} \; = 0 \tag{5}$$

Inserting Equation 3 into 5, and performing a substitution of variables with $\vec{X} = \vec{PQ}_{C} + \vec{\lambda}\vec{PQ}$" results in Equations 6 and 7. This expression is then evaluated for values of $\lambda_\forall = 0$ to produce the TLM equation displayed in Equation 8,

$$\frac{d}{d\lambda}\Big[\frac{\Delta(\vec{X})}{\Delta t_p} - F_{1D}(\vec{X})\Big] \mid_{\lambda_\forall = 0} \; = 0 \tag{6}$$

$$\frac{\Delta\vec{PQ}"}{\Delta t_p} - \vec{PQ}" \frac{\partial F_{1D}(\vec{X})}{\partial\vec{X}} \mid_{\lambda_\forall = 0} \; = 0 \tag{7}$$

$$F_{TLM}(\vec{PQ}") \equiv \frac{\Delta\vec{PQ}"}{\Delta t_p} = \vec{PQ}" \frac{\partial F_{1D}(\vec{PQ})}{\partial\vec{PQ}} \mid_{C}, \tag{8}$$

where C denotes the partial derivative across the 1-D model control state. The TLM of the 1-D photochemistry submodule linearizes the discrete model equations (2) that are derived from (1)

to enable a greater degree of accuracy when we compare results between the fully integrated 1-D model with calculations from its TLM.

Discretising Equation 8 across the 1-D model timesteps enables the TLM to evaluate the evolution of perturbations to the MMR vector in parallel with the control model run by using variable values that appear in the control state, displayed in Equation 9:

$$\vec{PQ}^{t+1}{}" = \vec{PQ}"^{t} + \frac{\Delta \vec{PQ}"}{\Delta t_p}\Delta t_p \quad , \tag{9}$$

which can be rearranged to highlight its structure as a matrix equation (Equation 10):

$$\vec{PQ}^{t+1}{}" = \left(\mathbf{I} + \Delta t_p \frac{\partial F_{1D}(\vec{PQ})}{\partial \vec{PQ}} \mid_C \right) \vec{PQ}"^{t} = \mathbf{A}_t \times \vec{PQ}^{t}", \tag{10}$$

where the TLM matrix, $\mathbf{A}_t$, is constructed from control run MMR values at timestep t. Multiplication by the perturbation vector $\vec{PQ}^{t}$ advances the perturbed state to the subsequent 1-D model timestep.

The MMR perturbation vector $\vec{PQ}"$ is of size N, and holds the perturbation in units of kg/kg of all I trace gas species and across all L model layers. So that for the TLM used in this work, the perturbation vectors are of length $N = L \times I = 25 \times 27 = 675$. Element $[(i \times l), (j \times m)]$ of the TLM matrix $\mathbf{A}_t$ denotes the gradient of the MMR of tracer species *i* at model layer *l* with respect to the MMR of tracer species *j* at model layer *m* at timestep t. This creates a matrix of size $N \times N$, where N=675 in our work. Extending Equation 10 to some arbitrary initial timestep provides an expression for the transition matrix, $\mathbf{R}$:

$$\vec{PQ}^{N}{}" = \prod_{t=-N}^{0} \mathbf{A}_{-t} \vec{PQ}^{0}{}" \equiv \mathbf{R}_N \vec{PQ}^{0}{}" \quad . \tag{11}$$

Comparison of the 1-D Photochemical Model and its TLM

We assess the accuracy of the TLM by comparing the perturbations to the control state integrated forward in time by the TLM with the same perturbation predicted by two separate runs

of the fully integrated 1-D model. If we define these runs as a function of initial conditions, where $\vec{PQ}_C^{t=0}$ is the initial control state and $\vec{PQ}_P^{t=0} = \vec{PQ}_C^{t=0} + \vec{\lambda}\vec{PQ}_C^{t=0}$ is the perturbed initial conditions for a vector of scalars $\vec{\lambda}$, the validity test is given by:

$$\lim_{\lambda_n \longrightarrow 0,\ \forall 1 \leq n \leq N} F_{1D}(\vec{PQ}_C^{t=0} + \vec{\lambda}\vec{PQ}_C^{t=0}) - F_{1D}(\vec{PQ}_C^{t=0}) = F_{TLM}(\vec{\lambda}\vec{PQ}_C^{t=0}) \quad . \tag{12}$$

The TLM model code uses double precision floating point mathematics whereas the 1-D photochemistry operates in single precision. We take these differences into account in our validity assessment by using a tolerance:

$$\frac{PQ_{i,l|P}^t - PQ_{i,l|C}^t}{PQ_{i,l|C}^t} \geq 1 \times 10^{-6} \quad , \tag{13}$$

where all variables are as previously defined.

Figure S1 shows four examples in which we compare the results from a brute-force perturbation of the 1-D model photochemistry, e.g. perturbing H_2O_2 in model levels 8–10, with the TLM approximation given by Equation 10. The magnitude of the perturbation λ is given by:

$$\lambda = \frac{m_{i,l,P}^{t=0}}{m_{i,l,Control}^{t=0}} - 1, \tag{14}$$

where i denotes the chemical species being perturbed, l denote the model vertical levels at which the species is perturbed. We compare mass mixing ratios from the two methods of perturbation over 144 physical timesteps (=three sols).

Generally, we find a strong linear relationship between the 1-D model and the TLM approximation, with slopes typically within 3% of the unit target value and Pearson correlation coefficients $\simeq$0.95 for a range of λ values. Small perturbations of H, OH, and HO_2 smaller than the precision criterion defined above are propagated by the TLM approximation but are not captured by the 1-D model that uses single precision.

Based on these calculations we conclude that our TLM represents a good linearisation of the fully integrated 1D chemistry model developed in (*3*) despite differences in the two models'

machine precision. The TLM enables us to develop high quality sensitivity analyses regarding the atmospheric state of Mars, and provides the basis of an accurate adjoint data assimilation scheme developed from the TLM.

1-D Photochemistry Adjoint

The adjoint model approaches takes advantage of the *adjoint property*, defined as $(\vec{x}, \mathbf{A}\vec{y}) = (\mathbf{A}^T\vec{x}, \vec{y})$. This property holds for a linear map $\mathbf{A}$ from vector $\vec{x}$ to vector $\vec{y}$, and the *adjoint* of this linear map $\mathbf{A}^T : \vec{y} \longrightarrow \vec{x}$, in which T denotes the matrix transpose.

The adjoint model is used to produce a gradient of sensitivities for a selected forecast element $J = PQ^{\Omega}_{i,l}$, representing the MMR of tracer *i* at model layer *l* at the desired forecast timestep *t* = Ω. The change in this desired element, ΔJ, is quantified by Equation 15. The change in the studied forecast element is the product of a) the change in MMR of tracer *i* at model layer *l* at timestep $0 \leq t \leq N$, $\Delta PQ^{\Omega}_{a,b}$ and b) the sensitivity of the forecast element to a change in the MMR, $\hat{J}^t_{a,b}$:

$$\Delta PQ^{\Omega}_{i,l} \equiv \Delta J = \sum_{a=1}^{I}\sum_{b=1}^{L} \frac{\partial J}{\partial PQ_{a,b}}^{t} \Delta PQ^{t}_{a,b} \equiv \sum_{a=1}^{I}\sum_{b=1}^{L} \hat{J}^t_{a,b}\Delta PQ^{t}_{a,b} \quad . \tag{15}$$

The adjoint of the 1-D photochemistry model is used to calculate the sensitivity vectors $\hat{J}$ across all prior model timesteps through the use of Equation 16:

$$\hat{J}^{t-1} = \mathbf{A}^T_{t-1}\hat{J}^t \quad . \tag{16}$$

which uses the transpose of the TLM matrices $\mathbf{A}_t$ and the adjoint property, defined above, to iterate the model *backwards* through time to mathematically quantify how sensitive the desired forecast element J is to the entire chemical constituency of the 1-D model control state at all previous model timesteps. Using the adjoint approach enables us to address questions such as "what changes in the photochemistry help explain the discrepancies between O_2 measurements collected by the Curiosity Rover and those predicted by GCM models (*4*)?"

First, we need to initialize the adjoint model equation (Equation 16) at the forecast time $t = N$. For a singular forecast aspect J taken at time $t = \Omega$, the only way a perturbation at time $t = \Omega$ could impact the value of J is if the perturbation were to be made to the aspect itself. The initial sensitivity vector $\hat{J}^{t=\Omega}$ will only have one non-zero element which will correspond to the location of the forecast aspect in the MMR perturbation vector $\vec{PQ}$". This non-zero value will be unity, due to this sensitivity element being equal to the partial derivative of J with itself, $\partial J/\partial J = 1$. As the sensitivity vectors are gradients of MMRs with respect to MMRs in this work, they can be regarded as dimensionless scale factors.

Evaluating the Adjoint Property of the TLM Matrix

The adjoint model is based upon the concept of the Adjoint Property:

$$(\vec{a}, \mathbf{A}\vec{b}) = (\mathbf{A}^T\vec{a}, \vec{b}) \quad , \tag{17}$$

which must be satisfied for Equation 16 to be valid.

In Figure S2, both sides of Equation 17 are calculated using TLM matrices to produce transition matrices $\mathbf{R}_t$, adjoint calculated sensitivity vectors $\vec{\hat{J}}_t$ using Equation 16, and initial perturbation vector $\vec{x'}^{t=0}$ from the same examples shown by Figure S1. The values of each side are calculated across 240 model timesteps (= 5 sols), and their differences calculated and displayed. Across all timesteps in all cases, the two sides of the adjoint property vary only at machine precision levels, highlighting that the adjoint property is valid for the TLM constructed here. This is an important test for the adjoint of our TLM because $\mathbf{R}_{N-1}^T$, the transpose of the transition matrix, does not necessarily equal $\mathbf{R}_{N-1}^{-1}$, the inverse of the transition matrix.

Temporal Invariance of Adjoint Results

If we take Equation 10 at the studied forecast time $t = N$, it can then be extended to examine the perturbed MMR vector at the forecast time $\vec{PQ}^N$" to the initial perturbed state $\vec{PQ}^0$" to

construct the transition matrix $\mathbf{P}_N$ (wquation 11).

If we rewrite Equation 15 using inner product notation and then insert Equation 11 we can use the adjoint property as a test of the reliability of the 1-D model adjoint method. Equation 18 shows that the perturbations in the initial MMR vector $\vec{PQ}^{0}$" result in the perturbation to the desired forecast element $\Delta J_N = PQ_{i,l}^N$ through the sensitivities calculated at the initial time $\hat{J}_{t=0}$:

$$\Delta J_N = (\mathbf{R}_N^T \vec{\hat{J}}_N, \vec{PQ}^{t_0}") \tag{18}$$

It then follows that as the transition matrix $\mathbf{R}^t$ can be defined at any desired timestep where $0 \leq t \leq N$, the value of ΔJ_N will be temporally invariant and can be evaluated at any model timestep.

Figure S3 examines the temporal invariance in the second example case study from Figure S1 for which O_2 has been perturbed across layers 1 and 2 with a magnitude of λ = 10^{-1}. We chose a forecast timestep of N = 144 (=3 sols). For all tracers i at layers l that experience a perturbation greater than 10^{-16} kg/kg in the 1-D model at this forecast timestep, we calculate the adjoint sensitivities of tracer i at layer l and the TLM perturbation vectors at each prior timestep $0 \leq t_0 < N$. We then calculate the adjoint perturbation values with corresponding values from the 1-D model, $\Delta J_N^{i,l}$. Figure S3 shows that for all trace gas species with perturbations at timestep N = 144 greater than 10^{-16} kg/kg, the adjoint method, using TLM calculated perturbations and adjoint calculated sensitivities, regularly achieves differences of less than 1%. We find these discrepancies are approximately invariant with respect to the backtrace timestep t_0. This calculation highlights that the adjoint is temporally invariant, yielding consistent results from all model timesteps.

2 Supplementary Text

2.1 Organic Products from the Accelerated Organic Chemical Network

Figure S4 shows the volume mixing ratio profiles (mol/mol) and column abundances (kg/kg) of CH_4 oxidation products calculated by the 1-D model when we force the photochemical lifetime of CH_4 below 400 m to be one hour. These include formaldehyde (HCHO), methyl hydroperoxide (CH_3OOH), formic acid (HCOOH), methanol (CH_3OH), methanediol ($HOCH_2OH$), and hydromethyl hydroperoxide ($HOCH_2OOH$). Where possible, we also show the theoretical detection limits for the Trace Gas Orbiter (TGO) NOMAD (Nadir and Occultation for MArs Discovery) and ACS (Atmospheric Chemistry Suite) spectrometer suites (*5, 6*).

The ACS low and high dust limits correspond to limits where the optical opacity of the atmosphere is set to $\tau = 0.2$ and 2, respectively. The detection limits in ACS solar occultation (SO) channels in these two dust conditions are 0.17 ppb and 1.7 ppb, respectively, which occur at approximately 2.5 km altitudes in the 1-D model. The NOMAD SO channels are more sensitive, with signal to noise ratios of 2000 and 3000 that correspond to detection limits lower to 0.04 and 0.03 ppb, respectively. These are reached at altitudes of 2.5–5 km throughout the Martian year, as calculated in the 1-D model.

NOMAD is the only TGO spectrometer with the capacity to observe column abundances of formaldehyde (HCHO). The limb nadir and solar Occultation (LNO) infrared spectrometer within the NOMAD suite and the ultraviolet/visible (UVIS) spectrometers have detection limits of 150 ppb and 16 ppb respectively, and the 1-D model calculates column abundances with magnitudes of 0.1 ppb, well below the detection limits.

CH_4 has theoretical detection limits provided by NOMAD and ACS (*5, 6*). ACS low and high dust condition limits in SO channels are 0.11 ppb and 0.97 ppb, respectively. The lower limit is reached at altitudes of roughly 5 km when the 1-D model is provided with a uniformly

distributed CH_4 VMR as prescribed by SAM (*7*) below altitudes of 400 m, and the higher limit in the high dust conditions is not achieved by the 1-D model at any altitude. The NOMAD solar occultations have detection limits of 0.025 ppb and 0.02 ppb with SNRs of 2000 and 3000, encountered at altitudes of 5–7.5 km. The NOMAD's UVIS spectrometer has theoretical column abundance detection limits of 11 ppb, which are not exceeded in our photochemical calculations.

Noting the topography of Gale Crater, the crater floor lies approximately 4.4 km below the Martian "sea level," the mean elevation across Mars' equator. Observed optical opacities do not commonly drop below $\tau = 0.3$ across the Martian year at Gale Crater (*8*). These factors, coupled with the low altitudes that the TGO detection limits are reached for HCHO and CH_4 in the 1-D model, implies that a highly reactive atmospheric environment for CH_4 could exist below the PBL at Gale Crater that contributes to the O_2 seasonal cycle whilst remaining undetectable by satellite observations in solar occultation and nadir modes.

3 Figures

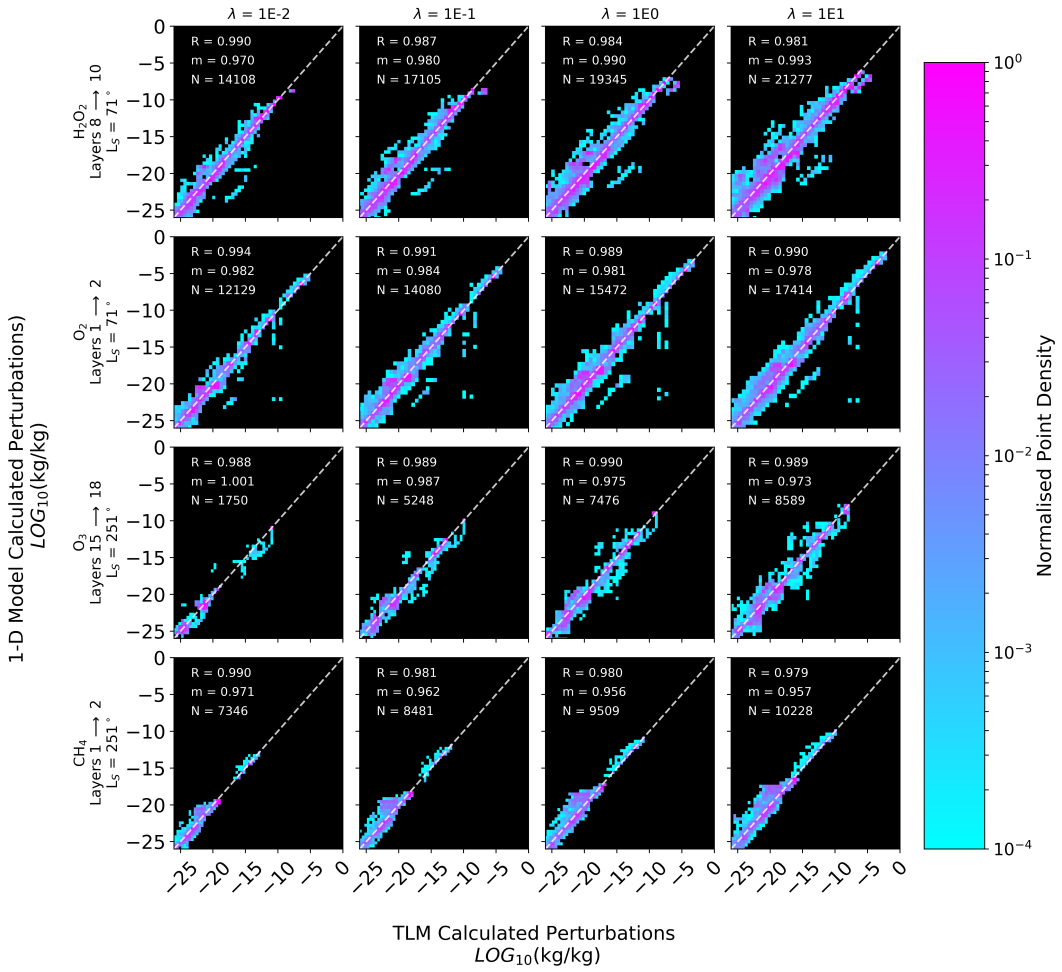

Figure S1: Comparisons of perturbations to all 27 trace gas species within the 1-D model calculated by the fully integrated 1-D model and those calculated by the TLM approximation. Initial perturbations are detailed on the left hand side, with perturbation magnitudes λ labeled on top of each column. Perturbations are tracked and plotted across 5 Martian sols (240 timesteps). The initially perturbed tracer species (i), the model layer (l) the initial perturbation is made at within the model, and the solar longitude of the cases are detailed on the y-axis. The initial magnitude of the perturbation, $\lambda = \frac{m^{t=0}_{i,l,P}}{m^{t=0}_{i,l,Control}} - 1$, is detailed along the top of the x-axis. R = Correlation coefficient, m = gradient of line of best fit, N = total number of data points.

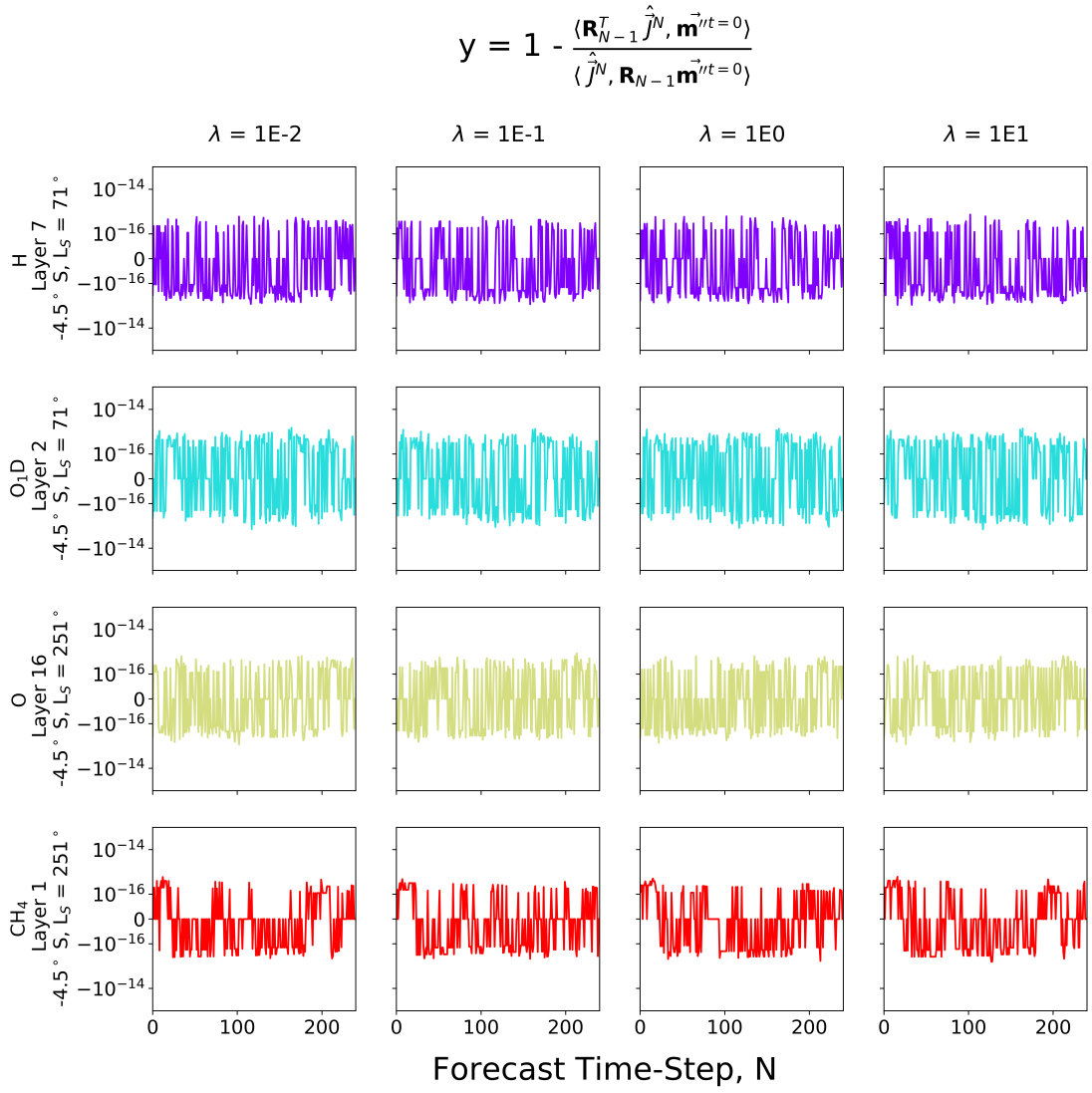

Figure S2: Adjoint property tests for each of the perturbation cases studied in Figure S1, using forecast elements as detailed on the left hand side. Each row corresponds to the respective test studied in Figure S1.

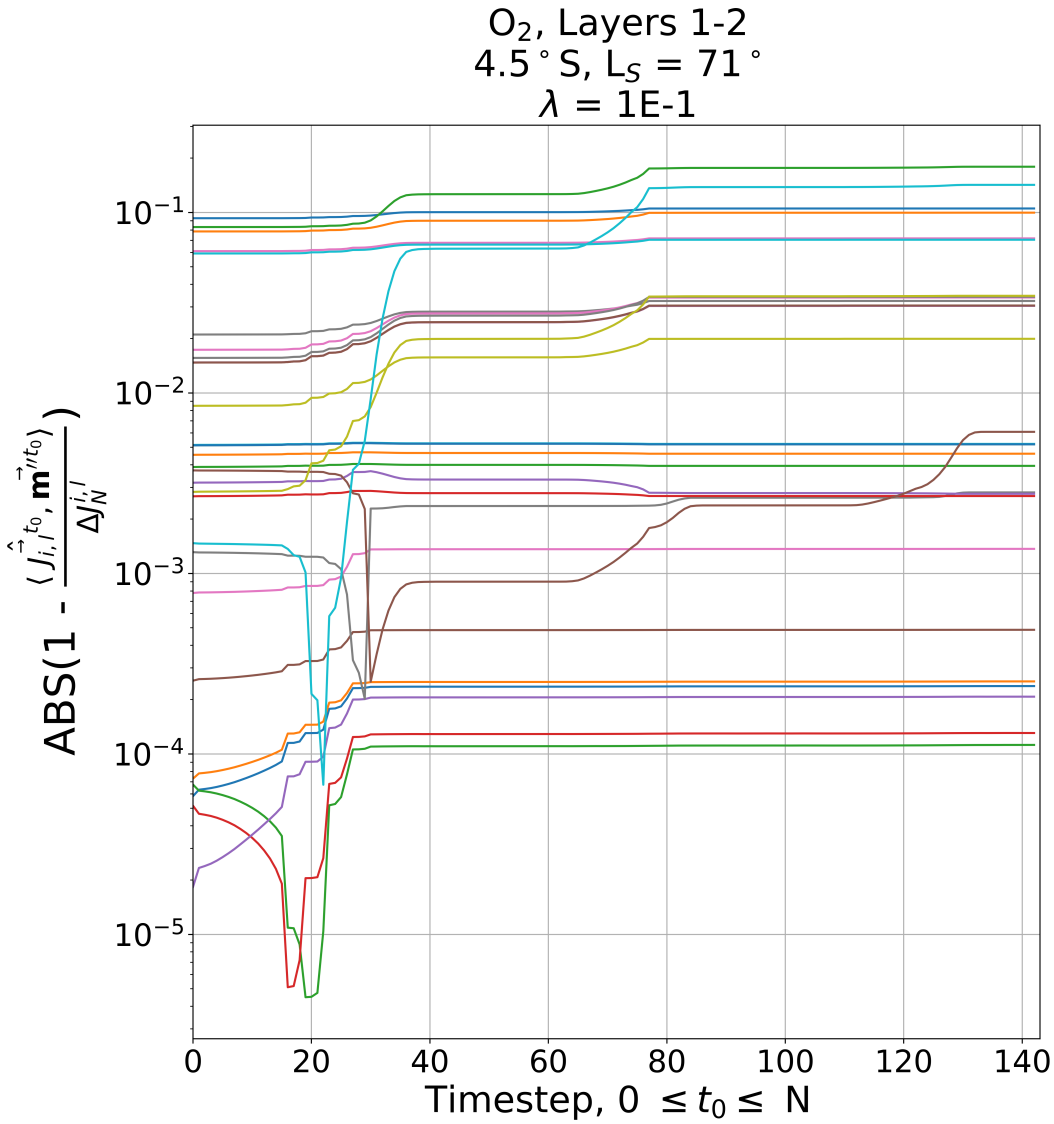

Figure S3: Temporal invariance of adjoint results. Each line corresponds to a model element with a forecast timestep perturbation value, $\Delta J_N^{i,l}$, greater than 10^{-16} kg/kg calculated via the adjoint equation, and its variance with respect to the 1-D model calculated value of $\Delta J_N^{i,l}$.

References

1. G. L. Mellor, T. Yamada, *Reviews of Geophysics and Space Physics* **20**, 851 (1982).

2. F. Forget, *et al.*, *Journal of Geophysics Research* **104**, 24155 (1999).

3. B. M. Taysum, P. I. Palmer, *Journal of Geophysical Research: Planets* **125**, e2020JE006491 (2020).

4. M. G. Trainer, *et al.*, *Journal of Geophysical Research: Planets* **124**, 3000 (2019).

5. A. C. Vandaele, *et al.*, *Space Sci. Rev.* **214**, 80 (2018).

6. O. Korablev, *et al.*, *Space Sci. Rev.* **214**, 7 (2018).

7. C. R. Webster, *et al.*, *Science* **360**, 1093 (2018).

8. S. D. Guzewich, *et al.*, *Journal of Geophysical Research (Planets)* **122**, 2779 (2017).

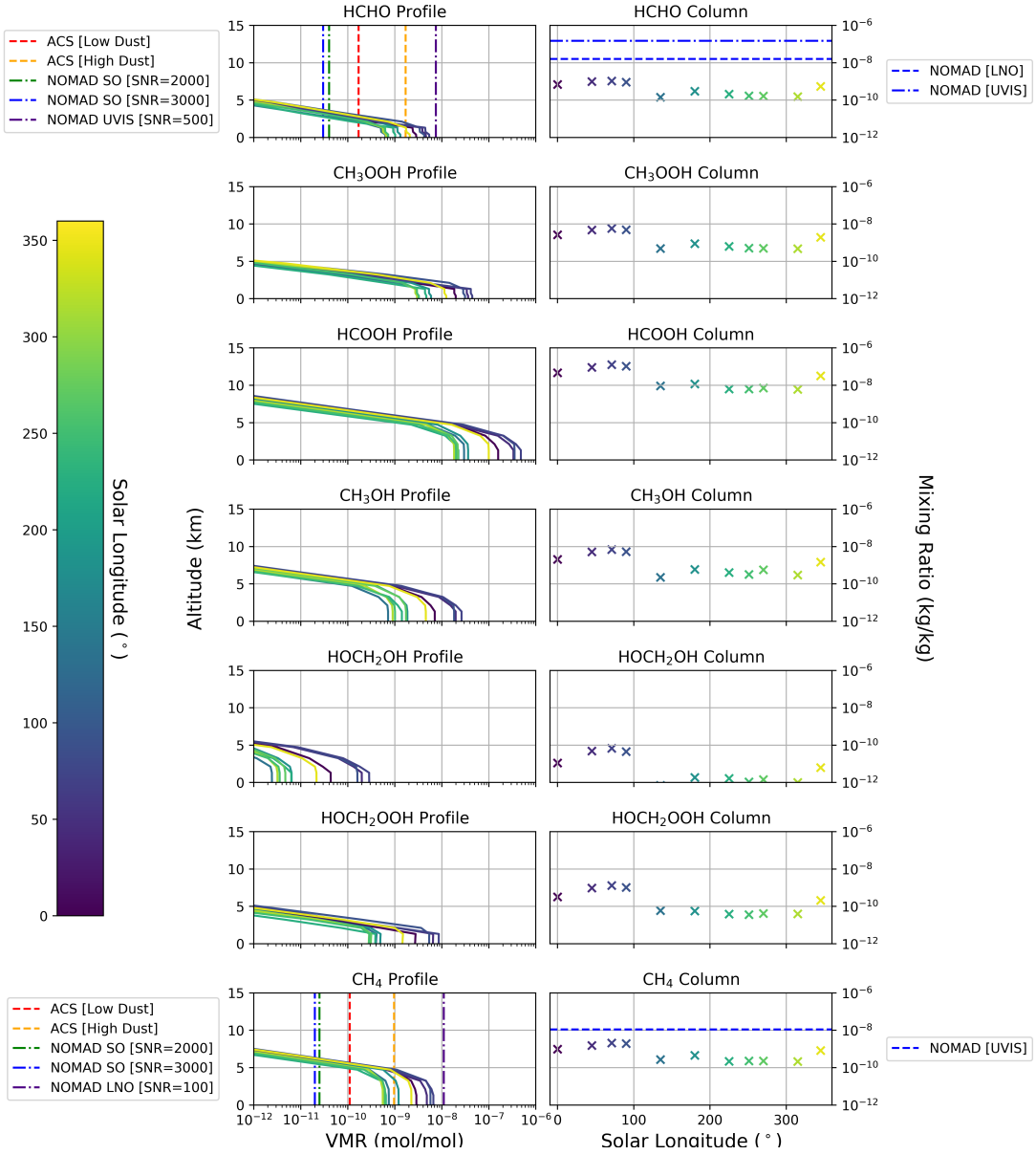

Figure S4: 1-D model organic products when initialised with SAM measurements of CH_4 concentrations at the surface, and a CH_4 photochemical lifetime forced to one hour below 400 m. Also shown are the theoretical detection limits of the ACS and NOMAD spectrometers aboard the ExoMars Trace Gas Orbiter, capable of measuring CH_4 and HCHO in solar occulation (profile) and nadir (column abundance) viewing modes.